

1 **Calibrated absolute seafloor pressure measurements for geodesy in Cascadia**

2
3 Matthew J. Cook¹, Erik K. Fredrickson², Emily C. Roland³, Glenn S. Sasagawa¹, David A.
4 Schmidt⁴, William S. D. Wilcock², and Mark A. Zumberge¹

5 ¹University of California San Diego, Scripps Institution of Oceanography

6 ²University of Washington, School of Oceanography

7 ³Western Washington University, College of Science and Engineering

8 ⁴University of Washington, Department of Earth and Space Sciences

9
10 Corresponding author: Matthew J. Cook (m4cook@ucsd.edu)

11 **Key Points:**

- 12 • Campaign-style surveys of in situ, absolute calibrated ocean pressure measurements were
13 made in the Cascadia subduction zone.
- 14 • These sensor-independent measurements act as long-term, absolute reference values that
15 can be used in future vertical deformation studies.
- 16 • We document the sources of error in the technique and quantify the formal uncertainties of
17 data collected from 2014 to 2017.

18 **Abstract**

19
20 The boundary between the overriding and subducting plates is locked along some portions of the
21 Cascadia subduction zone. The extent and location of locking affects the potential size and
22 frequency of great earthquakes in the region. Because much of the boundary is offshore,
23 measurements on land are incapable of completely defining a locked zone in the up-dip region.
24 Deformation models indicate that a record of seafloor height changes on the accretionary prism
25 can reveal the extent of locking. To detect such changes, we have initiated a series of calibrated
26 pressure measurements using an absolute self-calibrating pressure recorder (ASCPR). A piston-
27 gauge calibrator under careful metrological considerations produces an absolutely known
28 reference pressure to correct seafloor pressure observations to an absolute value. We report an
29 accuracy of about 25 ppm of the water depth, or 0.02 kPa (0.2 cm equivalent) at 100 m to 0.8 kPa
30 (8 cm equivalent) at 3,000 m. These campaign survey-style absolute pressure measurements on
31 seven offshore benchmarks in a line extending 100 km westward from Newport, Oregon from
32 2014 to 2017 establish a long-term, sensor-independent time series that can, over decades, reveal
33 the extent of vertical deformation and thus the extent of plate locking and place initial limits on
34 rates of subsidence or uplift. Continued surveys spanning years could serve as calibration values
35 for co-located or nearby continuous pressure records and provide useful information on possible
36 crustal deformation rates, while epoch measurements spanning decades would provide further
37 limits and additional insights on deformation.

38 **Plain Language Summary**

39
40 The Cascadia subduction zone has produced large earthquakes and tsunamis whose potential size
41 and interval is affected by the amount and distribution of locking between the tectonic plates. A
42 large portion of the subduction zone is offshore, where typical land- and satellite-based methods
43 are ineffective at measuring crustal deformation. Seafloor water pressure observations can be used
44 to monitor height changes, but pressure gauges inherently drift at rates typically exceeding
45 expected vertical seafloor deformation rates. The absolute self-calibrating pressure recorder
46

47 (ASCPR) measures the true, absolute, sensor-independent seafloor pressure by addressing and
48 correcting sources of error caused by the internal piston gauge calibrator and recording pressure
49 gauges. The accuracy of our measurements is about 25 ppm of the water depth, equivalent to 2.5
50 cm of height per 1,000 m of water. Campaign survey-style measurements using the ASCPR at
51 seven benchmarks off the coast of Newport, Oregon from 2014 to 2017 establish a long-term
52 record of absolute measurements that can be referenced by studies decades or more in the future
53 or can be used to estimate and correct drift of nearby continuous pressure gauges. Continued
54 measurements can provide more valuable information and insights on seafloor deformation and
55 thus locking in Cascadia.

56

57 **1 Introduction**

58 The Cascadia subduction zone poses considerable seismic and tsunami hazard to the coasts
59 of northwestern USA and southwestern Canada, stretching 1,300 km from Mendocino, CA to
60 Vancouver Island, BC (Walton et al., 2021). Large tsunamigenic earthquakes have ruptured along
61 the subduction zone numerous times in the past based on records of tsunami inundation, turbidite
62 flows, and paleoseismic evidence, most recently in 1700 (Atwater et al., 2005). The recurrence
63 interval of large earthquakes and tsunamis is suggested to be a few hundred years to a thousand
64 years; the current state of the subduction zone is not well-known (Atwater, 1987). More
65 information regarding the structure, deformation, and other properties of the subduction zone is
66 needed to better characterize the seismic and tsunami hazards in Cascadia. Although land-based
67 studies investigating interseismic and slow slip phenomena in Cascadia have been increasingly
68 common over the last decades, terrestrial data alone are insufficient for constraining properties in
69 the up-dip portion located offshore (Wang & Trehu, 2016).

70 Marine geodetic methods have been demonstrated over the last several decades. Acoustic
71 methods, notably GNSS-Acoustic, can measure horizontal motions at the cm-level, and have been
72 used to make measurements in various subduction zones, including Japan and Cascadia (Spiess et
73 al., 1998; Matsumoto et al., 2008). Seafloor pressure, a proxy for seafloor height, is also widely
74 used to measure vertical crustal motion and deformation. To be useful for seafloor geodesy,
75 pressure variations caused by oceanic and atmospheric variations must be extracted from the
76 seafloor pressure measurements to reveal the tectonic signal of interest. Although standard
77 pressure gauges are capable of mm-level resolution, they are unreliable for measurements over
78 months-to-years due to inherent drift (Polster et al., 2009). Pressure gauge drift contaminates and
79 often exceeds long-term signals of interest and is difficult to reliably characterize. Methods to
80 correct sensor drift include mobile pressure recorder (MPR) surveys by ROV, which measure
81 pressure changes relative to a stable reference site (e.g., Stenvold et al., 2006; Chadwick et al.,
82 2006; Nooner & Chadwick, 2009; Nooner & Chadwick, 2016), mobile pressure calibrator surveys
83 by ROV, which provide a controlled, calibrated pressure reference adjacent to long-term in situ
84 pressure recorders (Machida et al., 2020), normal self-calibrating pressure recorders (SCPRs),
85 which measure pressure changes relative to a piston-gauge calibrator (Sasagawa & Zumberge,
86 2013; Sasagawa et al., 2016), and A0A (also known as AZA) sensors, which measure pressure
87 changes relative to the internal air pressure (Wilcock et al., 2021).

88 The standard SCPR addresses gauge drift in situ by using a mechanical piston-gauge
89 calibrator (PGC) to intermittently produce a stable reference pressure close to the ambient seafloor
90 pressure. Drift in continuously recorded pressure gauges that are switched by a valve between the
91 ambient ocean pressure and the PGC reference pressure can then be accurately determined, and
92 the drift can be corrected. In this mode of operation, the actual value of the PGC reference need

93 not be known accurately, we only require that it remains stable for the duration of its deployment,
94 i.e., unknown but constant offsets are acceptable (Sasagawa & Zumberge, 2013; Sasagawa et al.,
95 2016).

96 An alternative use of the standard SCPR technology is to accurately account for every
97 measurement parameter in an absolute manner that is traceable to metrological standards and then
98 periodically deploy in a campaign style rather than continuously occupying one location. In this
99 fashion, a single instrument can be used to survey several locations. Because the absolute value of
100 the pressure on top of a benchmark is determined at each visit, we call this method the Absolute
101 Self Calibrating Pressure Recorder, or ASCPR. The instrument is carried and handled by ROV,
102 placed on a permanent seafloor benchmark (a concrete disc or similar platform), and alternately
103 records the ocean and the reference pressures for several hours. Knowledge of the reference
104 pressure's true value enables the absolute pressure on the benchmark to be determined. The
105 permanent benchmarks facilitate accurate re-positioning of instruments for all observations. Since
106 the pressures measured by the ASCPR are determined absolutely, each survey contributes to a time
107 series of point measurements and any future observations can be compared to earlier ones even if
108 different components or a different absolute sensor are used.

109 The absolute seafloor pressure measurements must be addressed within the context of the
110 overlying water column and atmosphere to isolate the tectonic signal. The ocean tides are aliased
111 in our records but can also be accounted for within a few cm through tidal predictions or models
112 (Agnew, 2012; Pawlowicz et al., 2012). Ocean variability at periods longer than the tides can be
113 aliased in each survey and present additional challenges. Averaging over many years can
114 ameliorate that problem, though a refinement to the method is to leave a continuously recording
115 bottom pressure recorder (BPR) at each benchmark to capture and account for seafloor pressure
116 variations attributed to these processes. Further improvements can be made by addressing these
117 processes using available regional pressure networks, satellite altimetry products, and CTD data
118 (Frederickson et al., 2019; Watts et al., 2021).

119 We conducted pressure surveys with an ASCPR along a trench-perpendicular profile in the
120 Cascadia subduction zone over a four-year period from September 2014 to September 2017. We
121 present the design and methods of the instrument and surveys, as well as absolute seafloor pressure
122 values, which will serve as longstanding fiducial values for future studies and estimated secular
123 rates. We also document the sources of error and report on the repeatability of the technique.
124

125 **2 Method**

126 The ASCPR instrument consists of a 40 cm diameter spherical pressure case that houses a
127 PGC (which generates a pressure by applying a mass force over a piston area), the mechanical
128 components needed to constrain the PGC mass during transit and deployment and spin the mass
129 during measurements, gimbals to level the PGC, two redundant quartz pressure gauges, and valves
130 to pressurize the PGC and alternately switch the gauges between the ambient seafloor and
131 reference pressures. The mass lock system prevents unwanted and potentially harmful torque on
132 the PGC system during transit. The mass spin-up system allows the PGC to generate a smooth,
133 continuous reference pressure and avoid pressure spikes caused by stick-slip behavior. The
134 spherical pressure case is mounted in a three-legged aluminum frame suitable for handling by an
135 ROV. Before each deployment a mass is loaded internally onto the system's piston of appropriate
136 size to create a reference pressure slightly less than the local seafloor pressure. This allows the
137 hydraulic connection to ambient sea pressure to pressurize the PGC, obviating the need for a high-
138 pressure pump, and minimizes the likelihood and amount of detectable hysteresis. In the survey

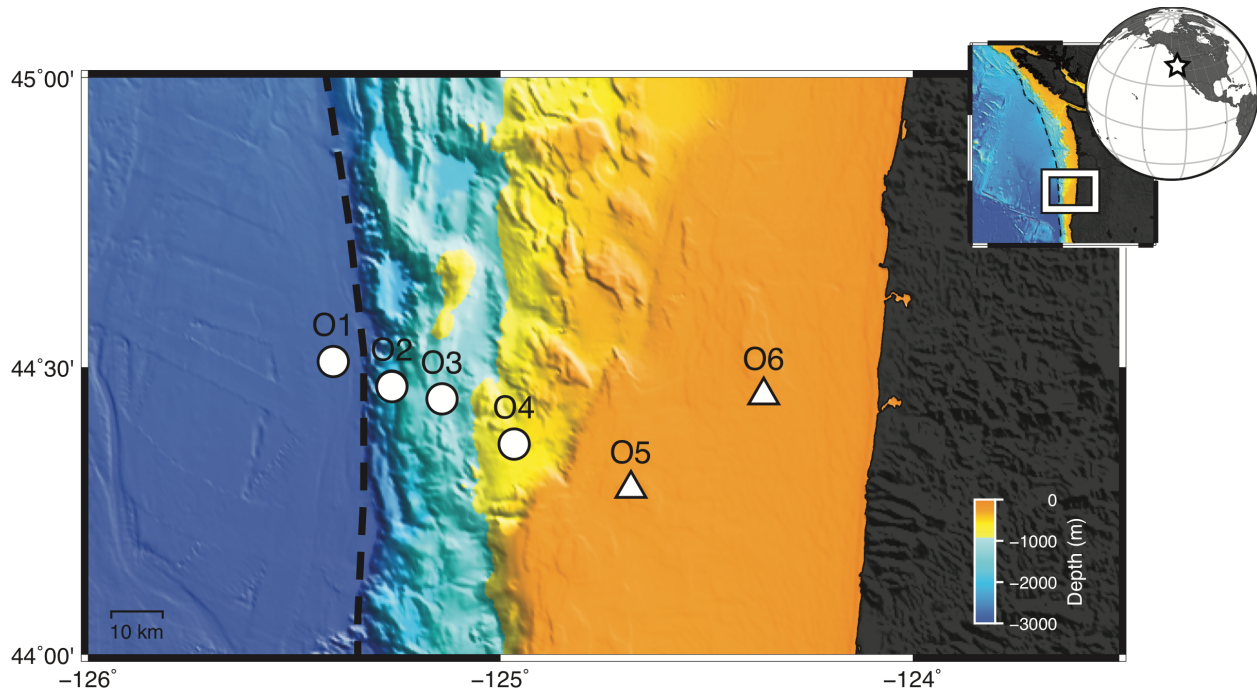
139 reported on here, the mass was transferred in the vessel's freezer held at seafloor temperature and
140 the instrument was kept there during transits between sites to help minimize thermal effects during
141 the measurement.

142 The ASCPR is turned on while connected to the ROV on the ship deck and starts recording
143 pressure data, ancillary measurement data, and state-of-health data at 1 Hz. The ROV carries the
144 ACPR to depth in the basket. Once on site, the ROV places the ASCPR on top of a pre-deployed
145 seafloor benchmark and remains in place, electrically connected to the instrument, for the duration
146 of the measurement. An operator on the vessel sends commands to the system to actuate internal
147 gimbals to level the PGC, unlock the mass, pressurize the PGC, engage the rotation mechanism to
148 spin the mass (this ensures the PGC is in a state of kinetic friction to minimize pressure spikes
149 caused by stick-slip behavior), and control the valve which alternates the quartz gauges between
150 sea pressure and PGC pressure. Gauge drift and errors are present in the gauge output, whether the
151 gauge is observing the reference pressure or ambient seafloor pressure. Alternating the gauge
152 output between the PGC reference pressure and ambient seafloor pressure allows us to apply
153 corrections determined from the reference pressures to the seafloor pressures. Ambient sea
154 pressure is buffered by a tube containing sebacate oil to prevent seawater from entering the PGC.
155 A typical measurement period spans about two hours, with five to seven cycles alternating between
156 10- to 15-minute-long seafloor and reference pressure observations.

157

158 **2.1 Survey profile**

159 The calibrated pressure surveys were conducted on seven concrete benchmarks at six sites
160 that form a trench-perpendicular profile off the coast of Oregon at 44.5° N (Figure 1, Table 1).
161 The farthest west station (O1) is located 105 km offshore on the Juan de Fuca Plate side of the
162 trench at 2900 m water depth. The other stations (O2, O2B, O3, O4, O5, and O6) are located on
163 the North American plate and are separated by approximately 15 km from each other towards
164 shore. The closest station to shore (O6) is about 20 km off the coastline at a depth of 70 m. Each
165 station had an autonomous, continuous BPR attached to the benchmark or located nearby. A
166 redundant benchmark (O2B) was established adjacent to O2 when a second set of BPRs was
167 deployed.



168
 169 **Figure 1.** Map of the survey area in the Cascadia subduction zone. The black dashed line indicates
 170 the deformation front at the foot of the accretionary prism. Circles represent standard benchmarks
 171 and triangles represent trawl-resistant benchmarks.
 172

173 Two types of solid concrete benchmarks were used depending on the water depth, expected
 174 seafloor material, and nearby trawling activity. The benchmarks located in deeper water (O1, O2,
 175 O2B, O3, and O4) are based on a design originally developed by Segawa and Fujimoto (1988) and
 176 later used in a variety of deep ocean settings (e.g., Chadwell, 2016). They have circular bases 76.2
 177 cm in diameter, 15 cm thick, with three 14 cm long legs protruding below, weighing a total of 66.7
 178 kg in water (145 kg in air). The shallow water benchmarks (O5 and O6) are a trawl-resistant design
 179 with a triangular base that slopes up to a platform 71.1 cm across and weigh 354 kg in water (770
 180 kg in air). Figure 2 includes photographs of each type of benchmark on the seafloor.

181 The benchmarks were coarsely leveled using the ROV manipulator to nudge them in a
 182 particular direction to within a few degrees of level. The total tilt of the benchmark is
 183 inconsequential if it is less than 10°, which is the amount of tilt the ASCPR gimbals can
 184 accommodate. The tilt at each benchmark was measured using the internal tiltmeter and recorded
 185 as a reference for future occupations to monitor the stability or potentially identify gross
 186 disturbances of the benchmarks (Table 1).
 187



188
189
190
191
192
193
194
195
196
197

Figure 2. Photographs of benchmarks. The left shows a standard circular benchmark at O1, a deep site (depth greater than ~400 m), and the right shows a trawl-resistant benchmark at O5, a shallow site (depth shallower than ~400m or located near known trawl zones).

Table 1. Basic station information. Benchmark tilts are listed as a reference for future occupations. Uncertainties are the quadrature sum of the tiltmeter accuracy and standard deviation of measurements conducted each occupation.

Station	Latitude (°N)	Longitude (°E)	Depth (m)	Benchmark tilt (°)	Established (year)
O1	44.5099	-125.4056	2907	4.0 ± 0.2	2014
O2	44.4670	-125.2636	1909	0.5 ± 0.1	2014
O2B	44.4661	-125.2637	1910	0.9 ± 0.1	2015
O3	44.4450	-125.1418	1315	3.4 ± 0.1	2016
O4	44.3666	-124.9670	620	0.3 ± 0.1	2016
O5	44.2889	-124.6838	79	3.4 ± 0.2	2016
O6	44.4512	-124.3616	70	3.0 ± 0.1	2016

198
199
200
201
202
203
204
205
206
207
208
209
210
211
212
213
214
215

2.2 Absolute determination of the PGC reference pressure

The ASCPR method relies on accurate determinations of the true, absolute value of the PGC reference pressure. The quartz-gauge observations of the PGC reference pressure reveal static offsets from imperfect calibrations and transients from thermal gradients, creep, or other unmodeled effects in the quartz gauges (Wearn & Larson, 1982; Polster et al., 2009). These offset and transient errors are present in the gauge output regardless of the gauges being directed to the reference pressure or ambient seafloor pressure. These errors are determined using the pressure difference between the actual, absolute, known PGC reference pressures and the observed gauge output during calibration intervals. Alternating the gauges between the PGC and ambient seafloor pressure allows us to apply the absolute gauge corrections to the seafloor pressure record as well. We do not expect any detectable hysteresis since our target reference pressure is chosen to be within about 200 kPa of the expected seafloor pressure. As a result, the seafloor pressure values are calibrated and traceable to absolute standards.

Equation 1 and Table 2 define the PGC reference pressure, P_{PGC} , and the significant variables (Bean, 1994). We measure and determine the absolute values and uncertainties of each correction term using NIST-traceable standards either prior to or during a deployment.

216

$$P_{PGC} = \frac{M \left(1 - \frac{\rho_{air}}{\rho_{mass}} \right) g \left(1 - \frac{\theta^2}{2} \right) + \gamma C}{A(1 + bP_0)[1 + 2\alpha(T - T_0)]} + P_{baro} \quad (1)$$

217

218 **Table 2.** Reference pressure variables and notes about their values and how they are determined
 219 or measured.
 220

Variable	Term	Comments
P_{PGC}	Pressure, PGC (kPa)	Piston gauge calibrator
M	Mass (kg)	Measured in lab (2016)
g	Gravitational acceleration (m/s ²)	Götze 2011 gravity formula + EGM2008 gravity anomaly + seawater gravity gradient
A	Piston area (m ²)	Fluke (2014)
θ	Tilt (rad)	Measured by Jewell 900 sensor; calibration of conversion coefficients done in lab (2014)
ρ_{air}	Internal air density (kg/m ³)	Calculated using ideal gas law for N ₂ , P_{baro}
ρ_{mass}	Mass density (kg/m ³)	Calculated using mass materials information
γ	Viscosity (m ² /s)	Nominal value of sebacate oil
C	Piston circumference (m)	Calculated from area value; Fluke (2014)
b	Coefficient of elastic deformation (1/Pa)	Fluke (2014)
P_0	Fluid pressure (Pa)	Calculated using simplified reference pressure ($P = Mg/A + P_{baro}$)
α	Linear coefficient of thermal expansion (1/°C)	Lab calibration (2018)
T_0	Reference temperature (°C)	Nominal value from DHI Fluke
T	Piston temperature (°C)	Measured by Fluke PRT; calibration of conversion coefficients done in lab (2016)
P_{baro}	Internal air pressure (Pa)	Measured by Vaisala PTB 110; conversion coefficients lab calibration (2016)

221

222 Table 3 provides the accuracy of each individual variable and the total measurement
 223 accuracy. Some of the terms in equation (1), such as temperature and internal air pressure, change
 224 on timescales shorter than the duration of a calibration, and are measured in situ.

225

226

227

228

229

In shallow waters, typically 100 m to a few hundred m deep, the primary error constituents are the internal air pressure and then the piston-cylinder cross-sectional area. The internal air pressure has an accuracy of 0.02 kPa within the nominal range and our operating range, corresponding to up to 20 ppm (at 100 m water depth). The piston-cylinder cross-sectional area for the larger diameter apparatus used for smaller pressures and shallower water depths has a

230 manufacturer provided accuracy of 14 ppm, which corresponds to about 0.01 kPa at 100 m water
 231 depth, or 0.1 kPa at 1,000 m water depth. Other errors are small on the order of a few ppm and
 232 contribute a small fraction of the total error.

233 At greater depths of several hundred m to several km, the error is dominated by the piston-
 234 cylinder area. The internal air pressure accuracy remains 0.02 kPa but constitutes a significantly
 235 smaller error contribution of 2 ppm (at 1,000 m depth) or less. The piston-cylinder used for greater
 236 depths and pressures is a smaller diameter and has a lower cross-sectional area accuracy of about
 237 25 ppm. As the water depth and reference pressure increase, the error also increases, reaching
 238 nearly 0.8 kPa at 3,000 m. The greatest improvement to our deep water measurements would be
 239 improving the accuracy of the piston-cylinder area, but that requires micrometer-level
 240 measurements of the piston-cylinder dimensions. Facilities equipped to do this are rare and
 241 prohibitively expensive. The error is otherwise the same as the shallow depths, where most of the
 242 remaining errors are small and contribute little to the total error.

243
 244 **Table 3.** Uncertainties of each reference pressure variable (or collective term) and the total
 245 quadrature sum error of a resulting calibration measurement. Some uncertainties scale with
 246 pressure (depth) while others do not. Three example depths are provided to highlight the
 247 uncertainty magnitude at various pressures (depths). A 10 ppm uncertainty at 1,000 m depth
 248 corresponds to 1 cm in height.
 249

Name	Variable	Accuracy	Example depth		
			100 m	1,000 m	3,000 m
Mass	M	(Minimum 14.648 kg) 0.9 ppm	3.7 ppm	4.3 ppm	0.9 ppm
		(Maximum 3.029 kg) 4.3 ppm			
Gravitational acceleration	g	2.3 ppm	2.3 ppm	2.3 ppm	2.3 ppm
Piston area	A	(PC-7300-200) 14 ppm	14 ppm	25 ppm	25 ppm
		(PC-7300-2) 25 ppm			
Thermal expansion	$[1+2\alpha(T - T_0)]$	4.1 ppm	4.1 ppm	4.1 ppm	4.1 ppm
Buoyancy	$\left(1 - \frac{\rho_{\text{air}}}{\rho_{\text{mass}}}\right)$	(Stainless Steel Mass) 1.5 ppm	3.3 ppm	1.5 ppm	1.5 ppm
		(Aluminum Mass) 3.3 ppm			
Tilt	$\left(1 - \frac{\theta^2}{2}\right)$	1.6 ppm	1.6 ppm	1.6 ppm	1.6 ppm
Elastic deformation	$(1+bP_0)$	(PC-7300-200) 1.1 ppm	1.1 ppm	0.1 ppm	0.03 ppm
		(PC-7300-2) 0.03 ppm			
		(PC-7300-200)	2 ppm	0.5 ppm	0.17 ppm

Surface tension	γ_C	0.002 kPa			
		(PC-7300-2)			
		0.005 kPa			
Internal air pressure	P_{baro}	0.02 kPa	20 ppm	2.0 ppm	0.67 ppm
Quadrature Sum Total	—	—	25.5 ppm	26.0 ppm	25.6 ppm

250
251
252
253
254
255
256
257
258
259
260
261
262
263

The values used to determine the reference pressure at each station and typical ranges for measured variables are provided in Table 4, while the exact values can be found in the ancillary data. For example, the barometric pressure within the sphere typically changes by 5-10 kPa during a calibration owing to the changing temperature inside the sphere. The internal temperature increases because of the electronics inside that are turned on when a survey is initiated, and a measurement sequence begins.

Table 4. Values used to determine the known reference pressure at each station. Tilt, piston-gauge temperature, and internal air pressure are measured in situ. Their values vary between each occupation and can fall within a broad, nominal range that is listed; however, they typically fall within a narrower range that is also specified. Their exact values can be found in the ancillary data records.

Variable	Value at Station				
	O1	O2 / O2B	O3	O4	O5 / O6
M (kg)	14.648207	9.539057	6.544407	3.029427	3.509207
g (m/s ²)	9.80496	9.80522	9.80540	9.80553	9.80555
A (10 ⁻⁶ m ²)	4.901758				49.02159
θ (10 ⁻³ rad)	Ranges from (-1.7, 1.7) but typically within (-0.87, 0.87)				
ρ_{air} (kg/m ³)	Ranges from (0.71, 1.03) but typically within (0.81, 0.95)				
ρ_{mass} (kg/m ³)	7779.907	5586.182	7613.153	3324.631	3230.054
γ (m ² /s)	0.031				
C (10 ⁻³ m)	7.84839				24.8198
b (10 ⁻¹³ 1/Pa)	7.54				12.6
P_0 (kPa)	29,372 +/- 10	19,153 +/- 10	13,163 +/- 10	6,132 +/- 10	774 +/- 10
α (10 ⁻⁶ 1/°C)	3.9				
T_0 (°C)	20				
T (°C)	Ranges from (4.5, 9.5) but typically within (5, 8.5)				
P_{baro} (kPa)	Ranges from (60, 85) but typically within (67.5, 77.5)				

264
265
266
267
268
269
270
271
272

The pressure observed by the gauges while valved to the ambient seawater is denoted $P_{\text{sea}}^{\text{obs}}$ and contains the tectonic vertical deformation signal of interest, as well as any variation in the overlying water column. The pressure observed while valved to the PGC is denoted $P_{\text{PGC}}^{\text{obs}}$. Each differs from their absolute counterparts, P_{PGC} and P_{sea} respectively, by the same error, P_{error} , attributed to imperfections mentioned above.

$$P_{\text{PGC}}^{\text{obs}} = P_{\text{PGC}} + P_{\text{error}} \quad (2)$$

$$P_{sea}^{obs} = P_{sea} + P_{error} \quad (3)$$

The gauge error, P_{error} , is equal to the difference between the observed calibration pressure and the true calibration pressure.

$$P_{error} = P_{PGC}^{obs} - P_{PGC} \quad (4)$$

We chose to model P_{error} as a constant offset and a relatively small, time varying component modelled with combined exponential and linear terms (Wearn & Larson, 1982; Watts & Kontoyiannis, 1990; Polster et al., 2009). Other numerical drift models exist, but the exponential component of a few cm sufficiently captures any short-term transients caused by viscoelastic creep or thermal effects, and the long-term linear component represents any long-term mechanical creep, outgassing, or aging of the quartz crystal (Paros & Kobayashi, 2015a). The exponential component is modeled starting at the initial time, t_0 , of the first calibration interval for an occupation and extending until the last time of the final calibration interval, with an amplitude, A , and time constant, B , typically on the order of a few minutes. The linear rate, C , is also modeled relative to the initial time, t_0 , and the offset is simply determined as D .

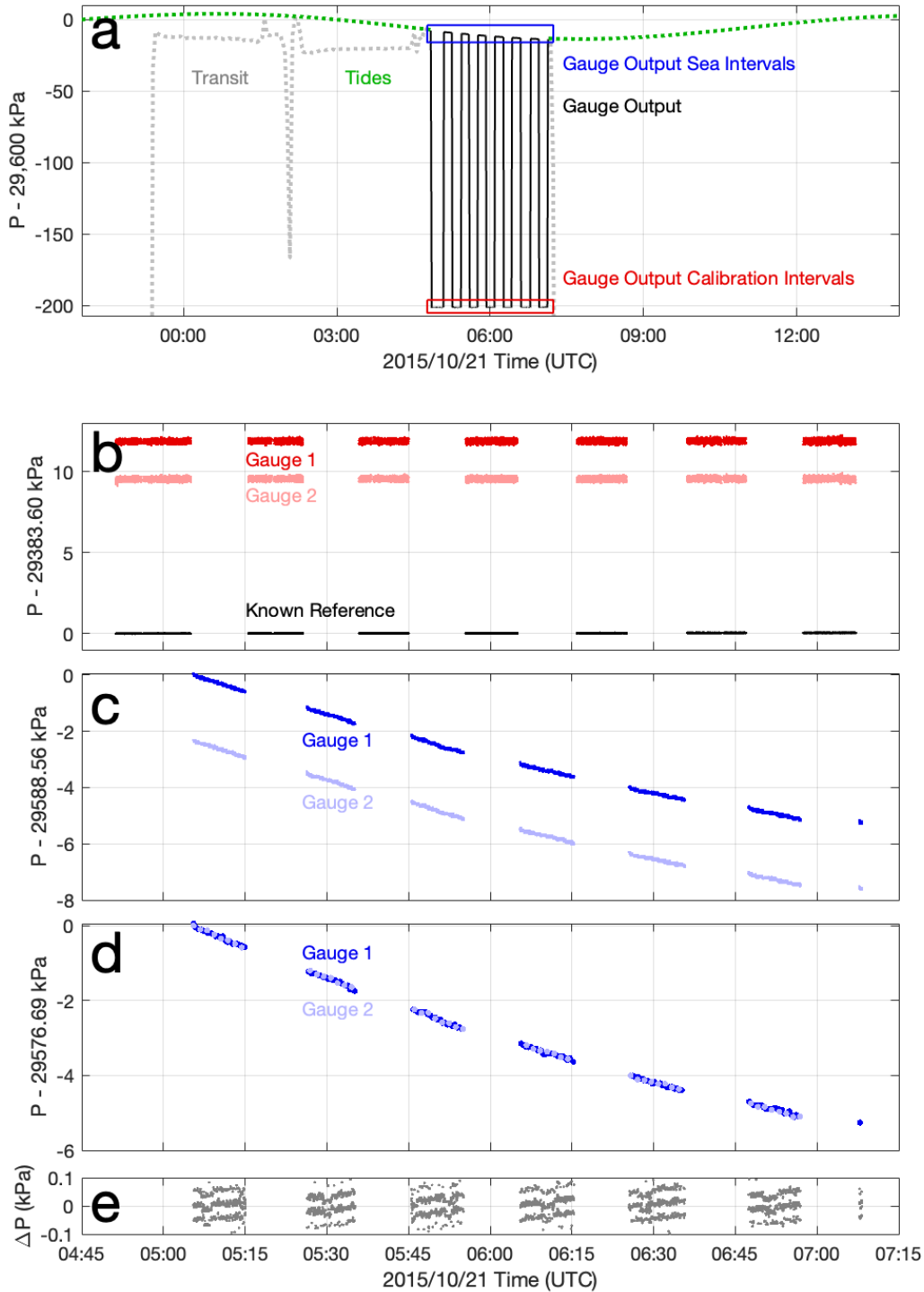
$$P_{error} = Ae^{-\frac{t-t_0}{B}} - C(t - t_0) + D \quad (5)$$

A non-linear least squares regression is used to calculate the best-fit coefficients and drift model to the gauge error time series defined as the difference between P_{PGC} and P_{PGC}^{obs} . The true sea pressure is computed by correcting P_{sea}^{obs} with the modeled error function, which is the same whether the valve connects the gauges to the PGC or the ambient ocean.

2.3 Absolute pressure occupation

Pressure time series show fluctuations related to the descent of the ASCPR to the seafloor and the flipping of the value between ambient and reference pressures (Figure 3). In (a), the pressure observed by one of the two redundant gauges over the course of a survey is plotted in grey (before and after a calibration) and black (during a calibration). The grey trace reveals that the instrument was taken to depth by the ROV just before 21 October 2015 at 00:00 and placed on the benchmark around 04:45 where, being stationary, it began to show the tidal pressure variation. The dotted green trace shows the predicted ocean tides. Soon after being emplaced on the benchmark, the gauges were alternately valved between the ambient seawater and the PGC reference pressure, the latter being around 200 kPa less than the sea pressure at this site. This creates an approximate square wave in pressure that covered seven valve cycles each lasting about 20 minutes. In (b), the raw observations of the two quartz gauges, P_{PGC}^{obs} , are plotted in red shades during the times they were valved to the PGC reference. The known output of the PGC (equation 1) as a function of time, P_{PGC} , is plotted in black at the same times (labeled “Known Reference” pressure). One can see that P_{error} is primarily an offset of about 12 kPa for gauge #1 and 9 kPa for gauge #2. The time variations in both the gauge records and the known PGC record are too small to be visibly discerned in this plot. In (c), the records from the two uncalibrated gauges are plotted during the periods when the valve connected them to the outside seawater, P_{sea}^{obs} ; the tidal signal is apparent. The offset between the two further exemplifies their imperfect calibrations, P_{error} . In (d), two P_{error} functions, determined independently for each gauge from the records shown in (b), have

318 been added to the two corresponding records plotted in (c), yielding the final, absolutely calibrated
319 seafloor pressure records, P_{sea} . The traces from the two gauges lie on top of each other, as they
320 should confirming the agreement of the corrections. In (e), the small differences between the two
321 gauges are plotted partly confirming the efficacy of the method. A perfect calibration method for
322 two independent gauges sensing the same pressure source should entirely remove any differences
323 between the two records. The difference between the two calibrated pressure gauges is practically
324 flat at zero, although small coherent variations (apparent as stripes or steps) persist. These are
325 likely due to noise in the applied calibrations and a very small timing offset between the two gauges
326 but are inconsequential and treated as noise.
327



328
 329 **Figure 3.** Pressure records during a typical ASCPR measurement at station O1 in 2015. (a) Raw
 330 pressure gauge output before (dashed grey line), during (solid black line), and after (dashed grey
 331 line) occupying the station for a measurement. Predicted ocean tides for the station are shown
 332 (dashed green line). The gauge output during calibration intervals is in the red box, shown in
 333 greater detail in (b). The gauge output during ambient seafloor pressure intervals is in the blue box,
 334 shown in greater detail in (c). (b) Observed output of the two gauges during calibration intervals
 335 (dark and light red) and the calculated time series of the known reference pressure defined in

336 equation (1). The raw gauge output is different from the known reference by an offset and
337 exponential-linear drift function. (c) Observed output of the two gauges during ambient seafloor
338 intervals (dark and light blue). The raw gauge output is also different from the true, absolute
339 seafloor pressure by the same offset and exponential-linear function determined from (b). (d)
340 Absolutely calibrated seafloor pressures at the height of the bottom of the piston-gauge. (e) The
341 difference between the two calibrated pressure records (dark and light blue traces in (d)) as an
342 indication of the method efficacy. The difference is nearly flat and centered at zero, meaning the
343 independent corrections applied to each gauge effectively capture each gauge drift signal and
344 produce no differential signal. Coherent noise is still present, mostly attributed to noise in ancillary
345 data used in the corrections.

346

347 **2.4 Height correction**

348 As a final correction, the pressure values measured by the ASCPR must be transferred to
349 the height of the surface of the concrete benchmark, 32.6 cm below the height of the piston-gauge
350 (Figure 4). The in situ calibration of the quartz pressure gauges as described above establishes a
351 function, P_{error} , that, when added to the raw gauge outputs, gives values equaling the known
352 pressure at the height of the piston-gauge. While the quartz gauges are physically separated from
353 the piston-gauge and therefore experience a pressure difference from the associated pressure head,
354 this offset is included in P_{error} – that is, the corrections to the quartz gauges incorporate both the
355 gauge imperfections and the pressure head relative to the bottom of the piston-gauge. There is a
356 hydraulic line filled with sebacate oil in the internal system that emerges in seawater through a
357 port 12.1 cm below the bottom of the piston, and this port is 20.5 cm above the benchmark. The
358 pressure head correction from the calibrated pressure measurement and the benchmark is therefore:

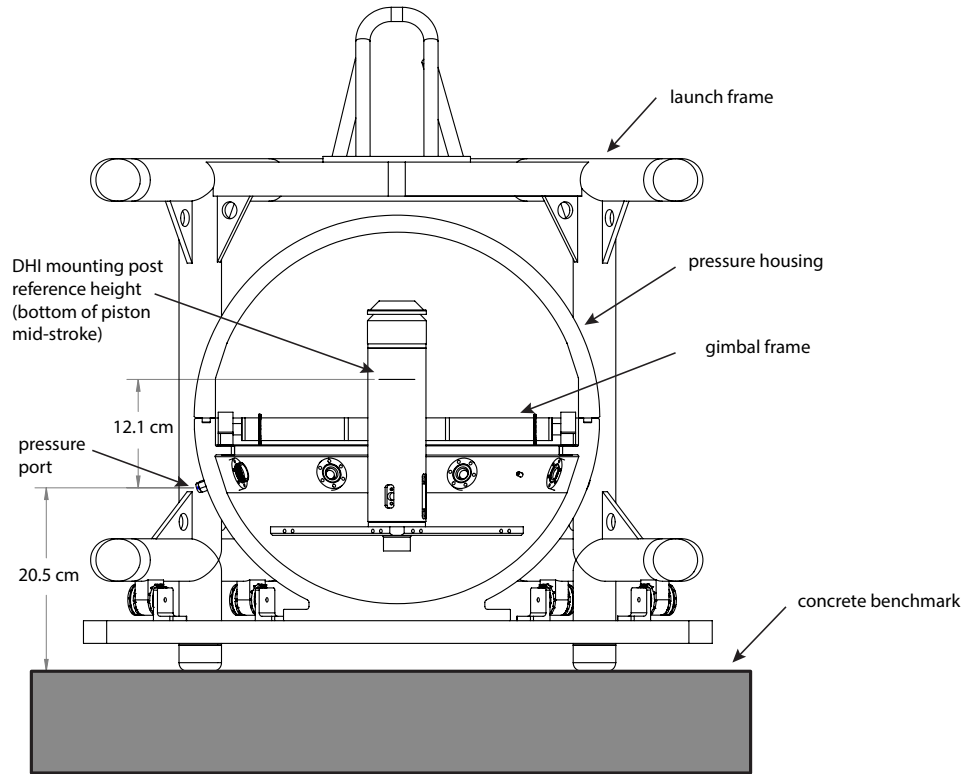
359

$$360 \quad \Delta P = \rho_S g \times 0.121 \text{ m} + \rho_W g \times 0.205 \text{ m}$$

361

362 where ρ_S and ρ_W are the densities of sebacate and seawater respectively, and g is the value of
363 gravity. Values for ρ_S and ρ_W are slightly site dependent because they depend on ambient pressure.
364 For ρ_S we use equation (2) from Paredes et al. (2012) assuming a temperature of 5 °C and standard
365 estimates for ρ_W . Table 5 lists the necessary terms and resultant height corrections for our sites.

366



367
 368
 369
 370
 371
 372
 373
 374
 375
 376
 377
 378

Figure 4. A cross-sectional drawing of the instrument in its spherical housing and frame. The height of the bottom of the piston-gauge is where the reference PGC pressure is determined. A correction to the benchmark 32.6 cm below depends on the fluid density in between, which is oil for part of the path and water for another portion. Note that the height of the piston bottom above the benchmark center varies only by an inconsequential amount in cases where the benchmark is not level.

Table 5. Terms used to determine the height correction for transferring absolute pressure measurements from the piston inside the ASCPR to the surface of the benchmark.

Station	Depth (m)	ρ_s (kg/m ³)	ρ_w (kg/m ³)	Gravity (m/s ²)	Height correction (kPa)
O1	2907	940	1041	9.80496	3.21
O2	1909	934	1036	9.80522	3.19
O2B	1910	934	1036	9.80522	3.19
O3	1315	931	1033	9.80540	3.18
O4	620	927	1030	9.80533	3.17
O5	79	925	1025	9.80555	3.16
O6	70	925	1025	9.80555	3.16

379
 380

2.5 Continuous pressure recorders

381 After removal of the ocean tides, physical oceanographic processes cause seafloor pressure
382 fluctuations that can eclipse tectonic signals of interest such as secular strain accumulation or slow
383 slip events (Frederickson et al., 2019; Watts et al., 2021). These processes include internal waves,
384 currents, eddies, El Niño Southern Oscillation (ENSO), and other decadal-scale events, which can
385 contribute 5 cm or more of noise at periods from hours to years (NRC 2012). When we infer the
386 seafloor height from the absolute pressure campaigns, we have aliased many of these
387 oceanographic processes. Some methods to reduce the oceanographic variability and noise include
388 using surrounding pressure data, specifically at a comparable depth, or satellite altimetry and CTD
389 data (Frederickson et al., 2019; Watts et al., 2021).

390 Co-located or nearby continuous pressure data can provide direct and valuable information
391 on the oceanographic signals that are otherwise aliased in our surveys. Over time spans shorter
392 than a couple decades, these data can provide significant improvements through direct
393 observations of oceanographic processes. Even though these signals tend to average out in long
394 time series spanning several decades, the data can still contextualize individual surveys.
395 Additionally, since ASCPR measurements produce accurate absolute seafloor pressure values, the
396 surveys can be used as calibration points to estimate and correct long-term linear drift in
397 continuous gauges. After correcting for drift, the full-rate continuous time series can be processed
398 to address oceanographic variability and used to estimate deformation rates. We deployed a
399 continuous BPR at or near each site to provide high-rate data during and between surveys. All the
400 BPRs used Paroscientific quartz pressure gauges but different sensor configurations were used to
401 accommodate different depths, durations, and logistical needs.

402 One BPR from the Applied Physics Laboratory (APL) at the University of Washington
403 (UW) was installed near station O1 on the OOI Cabled Array in September 2014. It housed a
404 Paroscientific model 46K pressure gauge in a titanium housing. Data were recorded at 1-sec
405 intervals and telemetered to shore in real-time to shore at the OOI Data Portal. An OOI Cabled
406 Array BPR was also installed as part of a Benthic Experiment Package near station O4, but the
407 sensor was changed, replaced, or out of service for most of the time spanning our surveys.

408 Two BPRs were constructed at the Scripps Institution of Oceanography (SIO) at the
409 University of California, San Diego (UCSD). These were deployed at the 1900 m depth site, O2.
410 They used battery powered Paroscientific model 46K pressure gauges inside aluminum pressure
411 cases. Data were integrated over 100-sec intervals and recorded to an internal memory card. The
412 data were recovered from the internal memory after the instruments were physically recovered.

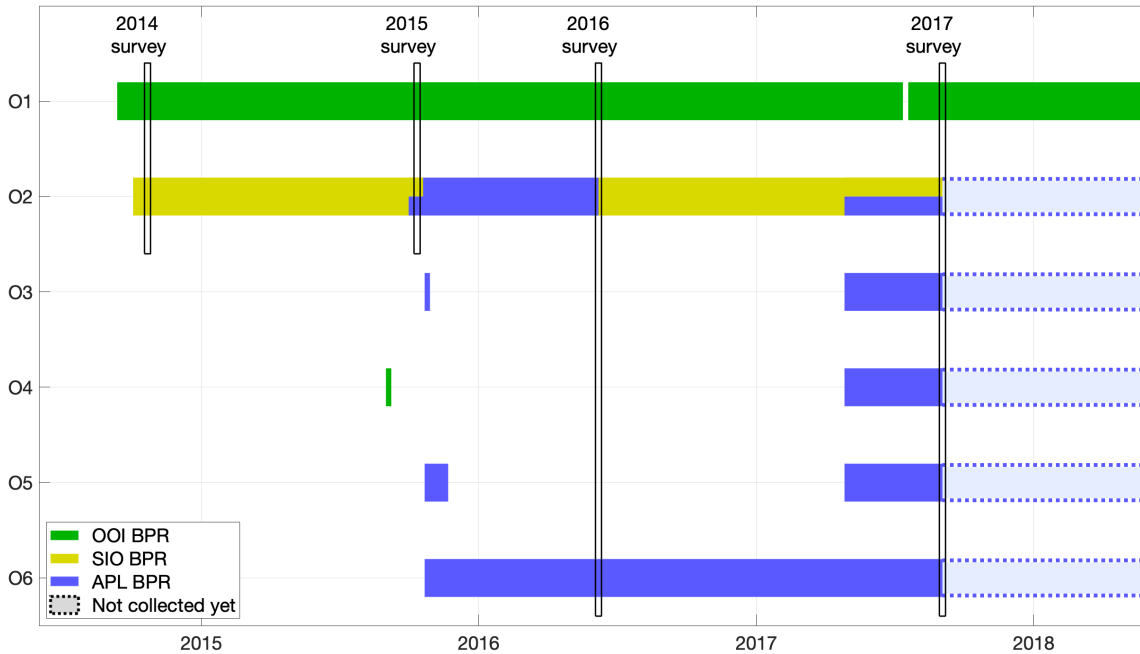
413 Another five BPRs were built by the UW APL. Two were designed for shallow water less
414 than 100 m depth (stations O5 and O6) and used Paroscientific model 2200A pressure gauges
415 inside PVC pressure cases. The other three were designed for greater depths ranging from 600 m
416 to 1900 m (stations O2, O3, and O4) and used Paroscientific model 31K, 42K, and 43K pressure
417 gauges housed inside titanium pressure cases. They all recorded at 15-sec intervals to internal
418 memory. Data were recovered wirelessly using a RF antenna linked to an ROV-held receiver a
419 few cm away to prevent disturbing the instruments when possible. In other instances, data were
420 recovered from internal memory after the instrument was recovered. These sensors were designed
421 to record for up to 10 years from when they were deployed.

422 The four separate BPR deployments at stations O2 and O2B lasted between 8 and 15
423 months and overlapped with the previous BPR by at least a few days. Although these records could
424 be concatenated to produce a single continuous record by matching the overlapping data intervals,
425 we are unable to reliably distinguish drift in the former record from drift in the latter record. The
426 linear drift rate could be estimated from data later in the record, but we have no way to estimate

427 the exponential drift, which is typically significant in the first 90 days, though longer exponential
 428 time constants have been observed (Polster et al., 2009). However, the records still provide
 429 observations and estimations of the oceanographic signals occurring during surveys but were not
 430 evaluated as a single, continuous record spanning all the surveys.

431 The BPRs at stations O3, O4, and O5 failed early on due to pressure housing leaks and we
 432 were unable to recover the continuous data for those sites. Therefore, continuous data at stations
 433 O3, O4, O5 are not included in this analysis since complete records were not available. The cause
 434 of the leaks was identified, and the instruments were modified and re-deployed. The BPR at O6
 435 did not fully span both surveys and had timing offsets difficult to reconcile. Therefore, O6 is also
 436 not included in this analysis.

437



438
 439

Figure 5. Timeline of continuous BPR data availability. ASCPR survey windows are boxed. Large gaps in the BPRs deployed at O3, O4, O5, and O6 are due to pressure housing leaks, which were identified, recovered, refurbished, and redeployed. The APL BPRs should be recording until about 2027 but data recovery requires an ROV or physical recovery. The OOI BPR has been recording continuously with only minor power interruptions.

445

446 2.6 Additional geodetic monumentation

447 Benchmarks placed on the seafloor acted as our primary measurement markers. In 2016,
 448 we deployed BPRs mounted to concrete seafloor benchmarks provided by APL near stations O2
 449 and O2B, O3, O4, O5, and O6. These secondary BPR benchmarks included a platform wide
 450 enough to place our instruments. In 2017, we installed secondary geodetic monuments, which
 451 consisted of 4-m-long, 4.8-cm-diameter aluminum pipes jettied between 3 to 6 m deep into the
 452 seafloor sediment so that about 1 meter extended above the seafloor, at O1, O3, and O4. The pipe
 453 is better coupled to the sediment and provides a stable comparison monument within a few meters
 454 of the primary benchmark. The pipe was painted with alternating 15.0 cm long black and yellow
 455 stripes to increase visibility and provide a vertical length scale. A 15.3 cm by 40.3 cm metal plate

456 with yellow-painted edges was fastened to the top of the pipe with a firehose coupling to support
 457 a pressure recorder.

458 An MPR was used to make a total of four alternating, 5-minute-long seafloor pressure
 459 measurements between the primary benchmark and secondary benchmark: either a pole-mounted
 460 plate or secondary concrete benchmark. Secondary monuments will provide a means in future
 461 surveys to assess the stability of the primary benchmarks by repeating the MPR surveys between
 462 them. The MPR baseplate dimensions are close to the secondary monument top plates, so when
 463 the MPR is placed centered on the plate, the uncertainty attributed to variations in placement is
 464 very small. The pressure difference, a proxy for height difference, was calculated after a computed
 465 tide model using Some Programs for Ocean Tide Loading (SPOTL; Agnew, 2012) and combined
 466 exponential-linear drift were removed from the short survey. Table 6 lists the pressure differences
 467 between the surface of the primary concrete seafloor benchmarks and the heights of the plates on
 468 the secondary benchmarks. A height difference between the two can be determined using the local
 469 gravity and seawater density.

470
 471 **Table 6.** Pressure differences between primary benchmarks and secondary geodetic monuments
 472 as measured by the MPR surveys. The difference is taken as the pressure at the primary benchmark
 473 minus the pressure at the secondary reference. Pressure uncertainties are single standard
 474 deviations.

475

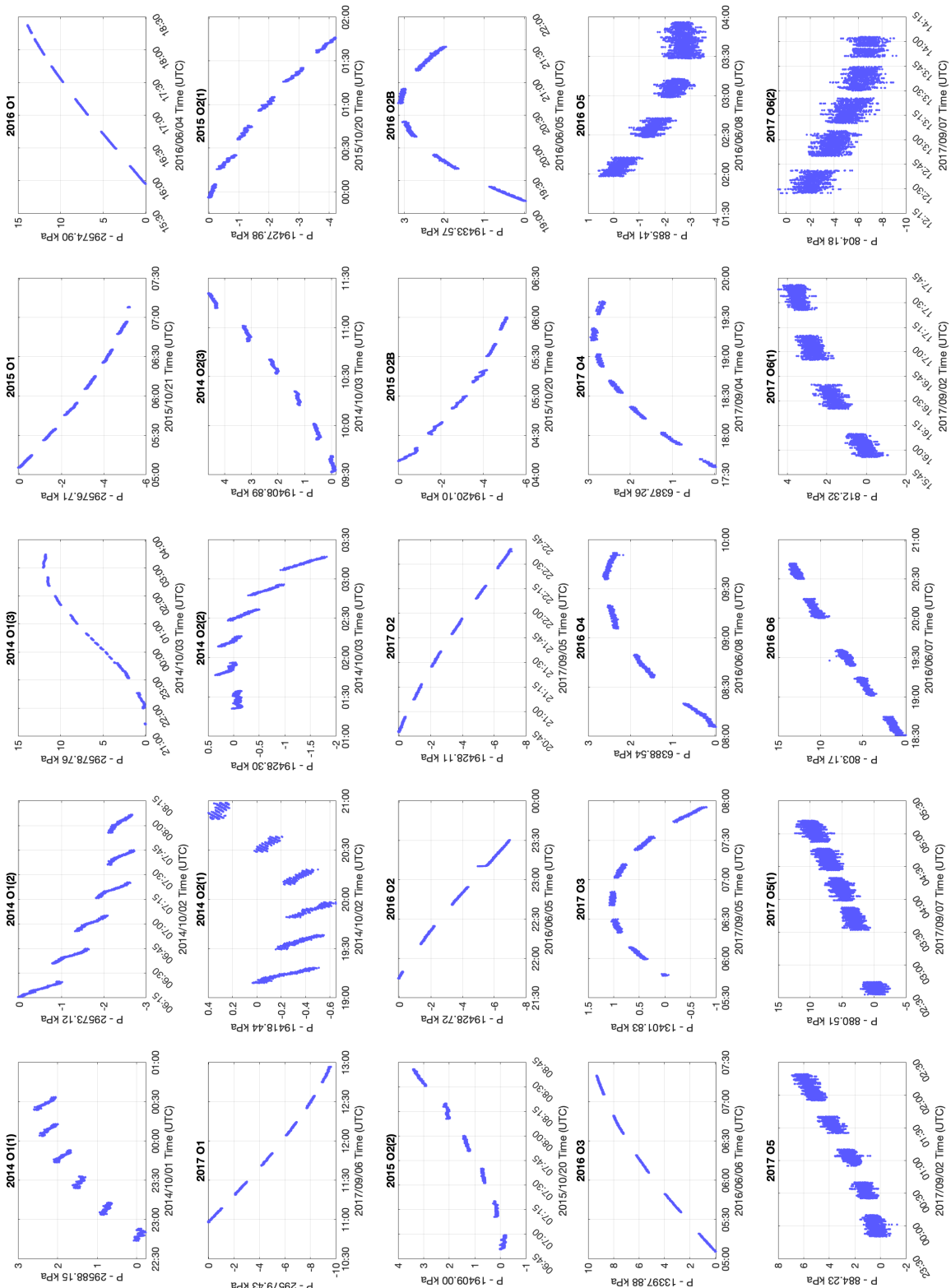
Station	Secondary Reference	Pressure Difference (kPa)
O1	O1-pole	10.0 ± 0.1
O2	O2B	-6.6 ± 0.1
O2B	O2-APL benchmark	6.5 ± 0.1
O3	O3-pole	12.6 ± 0.1
O4	O4-pole	2.9 ± 0.1
O5	O5-APL benchmark	-20.5 ± 0.1

476

477 3 Results

478 We present the results in three forms. First, Figure 6 plots the corrected absolute sea
 479 pressures at the instrument reference height of the PGC for each occupation at each station. The
 480 pressures can be transferred to the benchmark surface by applying the appropriate height correction
 481 (Table 4). Table 7 provides the absolute seafloor pressure value recorded at the specified date and
 482 time and at the height of the piston-gauge calibrator, not including the height correction described
 483 in section 2.4 nor any tidal corrections corresponding to the plots in Figure 6. Once corrected for
 484 the instrument's height to the benchmark surface and an estimated tidal correction, these values
 485 form the basis for future decadal-scale absolute seafloor pressure measurements, which can be
 486 used to infer motions caused by tectonic deformation and changes in the overlying water column.
 487 These instrument-independent, fiducial measurements form the foundation for long-term surveys
 488 and studies of secular rates caused by tectonics and sea level rise.

489



490
491
492
493

Figure 6. Corrected seafloor pressure records for each survey conducted at O1 through O6 between 2014 and 2017.

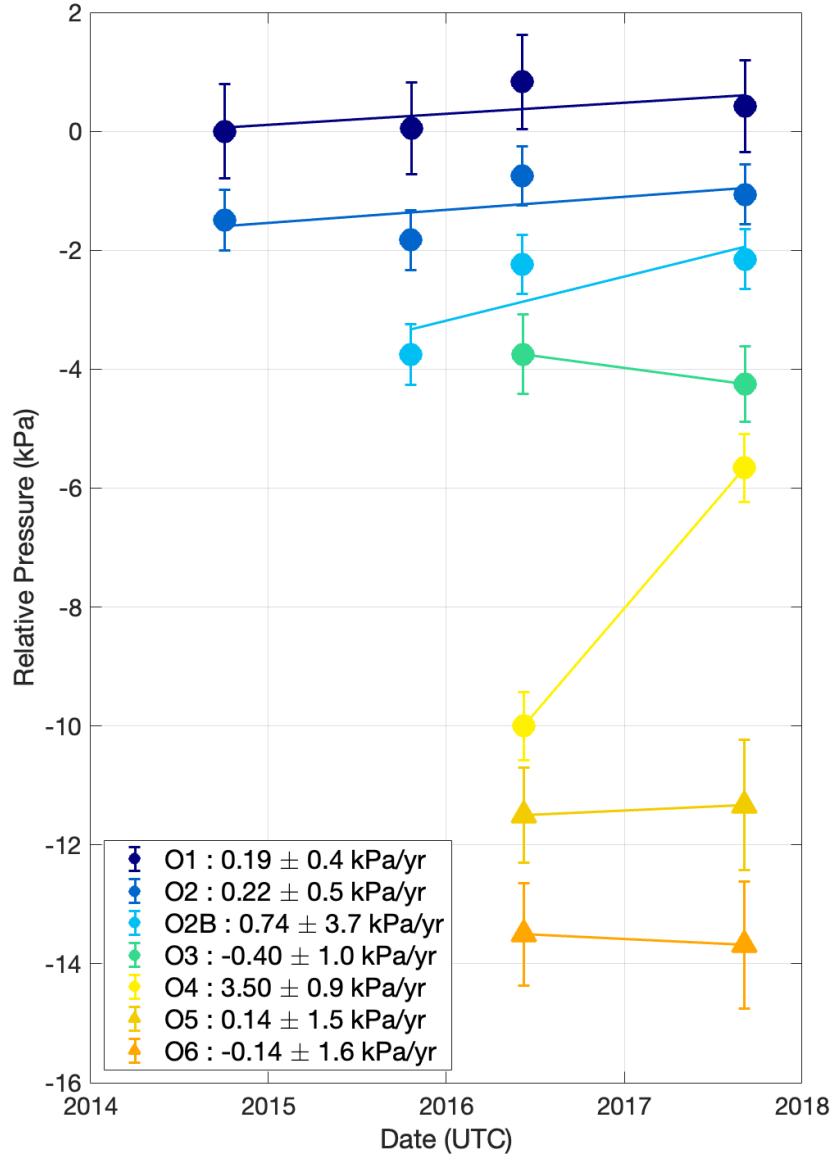
494 **Table 7.** Corrected ocean pressure values starting at the indicated date and time for each station.
 495 The duration of each survey is also provided. These values are also reflected in the plotted offsets
 496 shown in Figure 5. Uncertainties listed are the quadrature sum of the total PGC error and the RMS
 497 noise of the calibration pressure data.
 498

Date	Time (UTC)	Duration	Pressure, no tidal correction (kPa)
O1			
2014-10-01	22:43:55	1h50m	29,588.15 ± 0.8
2014-10-02	06:15:30	1h51m	29,573.12 ± 0.8
2014-10-03	21:25:30	6h03m	29,578.76 ± 0.8
2015-10-21	05:05:30	2h03m	29,576.71 ± 0.8
2016-06-04	15:57:15	2h25m	29,574.90 ± 0.8
2017-09-06	10:58:00	1h58m	29,579.43 ± 0.8
O2			
2014-10-02	19:09:00	1h50m	19,418.44 ± 0.5
2014-10-03	01:21:05	1h56m	19,428.30 ± 0.5
2014-10-03	09:31:35	1h51m	19,408.89 ± 0.5
2015-10-20	23:56:00	1h50m	19,427.98 ± 0.5
2015-10-20	06:50:50	1h50m	19,409.00 ± 0.5
2016-06-05	21:44:45	1h46m	19,428.72 ± 0.5
2017-09-05	20:47:30	1h52m	19,428.11 ± 0.5
O2B			
2015-10-20	04:10:30	1h50m	19,420.10 ± 0.5
2016-06-05	19:11:35	2h22m	19,433.57 ± 0.5
O3			
2016-06-06	05:05:35	2h15m	13,397.88 ± 0.4
2017-09-05	05:46:50	2h08m	13,401.83 ± 0.4
O4			
2016-06-08	08:05:45	1h47m	6,388.54 ± 0.2
2017-09-04	17:35:50	2h06m	6,387.26 ± 0.2
O5			
2016-06-08	01:58:30	1h58m	885.41 ± 0.1
2017-09-02	23:50:30	2h29m	884.23 ± 0.1
2017-09-07	02:33:00	2h39m	880.51 ± 0.1
O6			
2016-06-07	18:30:50	2h11m	803.17 ± 0.1
2017-09-02	15:55:45	1h45m	812.32 ± 0.1
2017-09-07	12:27:30	1h36m	804.18 ± 0.1

499
500
501
502
503
504
505
506
507
508
509
510
511
512
513
514
515
516
517
518
519
520
521
522
523
524
525
526
527
528
529
530
531
532
533
534
535
536

Second, we also provide estimated secular deformation rates using surveys as individual points in long-term time series (Figure 7). Each point is the average of the absolute seafloor pressure with a tidal correction generated by SPOTL applied and a station specific offset removed for visual clarity (Agnew, 2012). We use tides generated by SPOTL in lieu of tides computed using harmonic analysis of continuous pressure data (e.g., t_{tide}) for consistency between all stations and years since continuous pressure data are not available for every occupation (Pawlowicz et al., 2012). Error bars and uncertainties represent the single standard deviation quadrature sum of errors attributed to the instrument measurements and RMS of the corrected, de-tided seafloor pressure. Most of the uncertainty at deeper stations is attributed to instrumental effects while the uncertainty at shallow stations is dominated by oceanographic processes whose effects will average out over long time spans of decades or more. The uncertainty of the estimated rates is inversely proportional to the total time span of the data and thus will improve with future measurements.

The surveys at each station suggest modest rates of motion equivalent to a few cm/year or less in most cases. These rates may be larger than the expected tectonic signals in the region, but they also likely contain oceanographic components due to aliasing that we cannot quantify presently. Nonetheless, the estimated rates are within a reasonable range given the uncertainties and generally agree with expected deformation patterns, i.e., subsidence near the trench (stations O1, O2) and uplift closer to the coast (stations O5, O6). Station O4 (Figure 7, bright yellow circle trace) is an exception, where the two surveys suggest a rate of +3.5 kPa/year is occurring (equivalent to 35 cm/year of height change), a rate that is nearly 4 times the estimated uncertainty and much larger than that observed elsewhere. We could not identify any egregious source of instrumental error, nor do we have a solution to mitigate this error at Station O4. The instrument and all components are handled meticulously and maintained, but we investigated potential sources of error of this magnitude (e.g., a mass change of 2 g, barometer calibrations, etc.). If it were attributed to components such as the piston-gauge area being chipped, damaged, or deformed, then that would produce similar discrepancies in the other stations and surveys. During the 2016 campaign at station O4, the ASCPR was moved from the ship freezer to the ship deck and prepared for loading on the ROV. The pressure case sphere was not fully sealed, so the instrument was returned to the ship freezer and resealed, which may have inadvertently caused a thermal shock to some component not captured by internal sensors. During the 2017 campaign, while recording at station O4, the ROV unexpectedly lost thruster control and came off bottom and moved the instrument from its placement on the benchmark. The ASCPR was quickly issued commands to stop the mass rotation and lock it in place as to not damage the PGC. We do not believe that the PGC was damaged, as this would be reflected in other measurements as well, but this event may have introduced some other unmodeled error when we resumed the measurement. The high rate may have been caused by aliasing of some very strong oceanographic signal. However, additional surveys spanning a greater time will eventually converge toward a more accurate value.



537
538
539
540
541
542
543
544

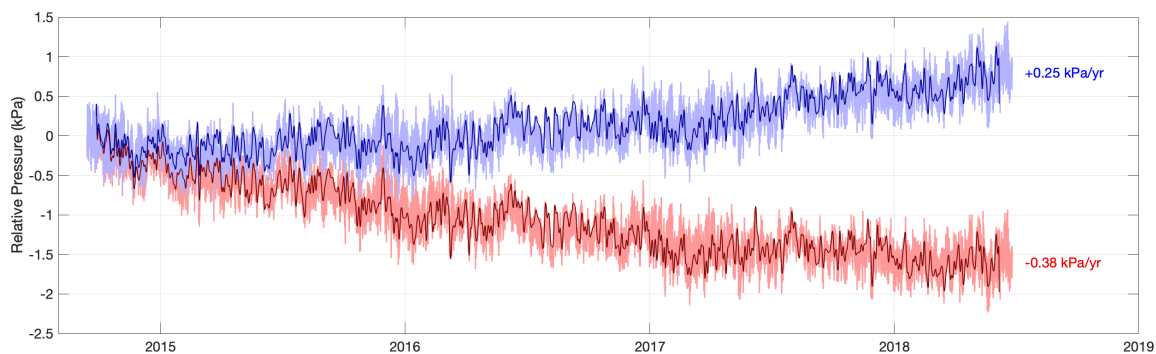
Figure 7. Pressure survey results from all stations. Estimated rates based on the individual surveys are listed. The plot shapes indicate the benchmark form factor (standard circular benchmark or triangular trawl-resistant benchmark). The inset legend provides the estimated pressure rates and uncertainties that were estimated by linear least squares fit. A pressure change of 0.1 kPa is equivalent to a height change of 1 cm.

545
546
547
548
549
550
551
552

Lastly, we leveraged our available continuous pressure data at station O1 to provide a better secular rate estimate. The ASCPR survey was treated as an individual calibration value used to calculate and remove only a long-term linear drift from the continuous record, which contains information on non-tidal oceanographic signals at periods shorter than the interval between surveys (8 to 12 months). Linear least squares fit to the difference between the overlapping absolute survey data and continuous BPR data was used to calculate the linear drift rate of the BPR, which was then removed from the continuous pressure record. The exponential component was not modeled because the small number of ASCPR surveys cannot sufficiently constrain it, and

553 the BPR was installed a few months prior to the first survey so the exponential component was
 554 likely less significant. The resulting drift-corrected pressure record was resampled to 30-minute
 555 intervals, de-tided using `t_tide` (Pawlowicz et al., 2012), and then lowpass filtered using a FIR
 556 filter with a passband at 1.2×10^{-6} Hz (0.10 cycles/day) and stopband at 7.7×10^{-6} Hz (0.067
 557 cycles/day). A linear deformation rate was estimated from the record by linear least squares.

558 Station O1 had a single continuous BPR that spanned all the surveys conducted. This record
 559 was calibrated as described in section 2.5. The secular rate for station O1 based on continuous
 560 BPR data corrected for gauge drift using the absolute pressure surveys as calibration points is
 561 estimated and plotted in Figure 8. The continuous records at the other stations were insufficient
 562 for this analysis at this time, described in section 2.5. However, the BPRs deployed in 2017 were
 563 designed to record for 10 years, so additional absolute pressure surveys conducted before 2027
 564 should allow those continuous data to be evaluated in this way.
 565



566
 567
Figure 8. Continuous pressure record at station O1. The raw, uncalibrated pressure time series for
 569 is plotted in red. The pressure times series corrected for long-term, linear drift using absolute
 570 pressure surveys as calibration values is plotted in blue. The calibrated record reveals a significant
 571 difference and therefore drift, which could be mistakenly interpreted as a physical signal. Arbitrary
 572 offsets are plotted for clarity.

573
 574 **4 Conclusions**

575 Absolute seafloor pressure surveys provide inherent value on their own as fiducial values.
 576 The ASCPR measurements can be used as longstanding benchmark values that can be incorporated
 577 into future geodetic studies. Each survey acts as a point in a long-term time series that could span
 578 decades or more and elucidate secular signals associated with tectonics or sea level rise.
 579 Additionally, the measurements' utility is improved if co-located with continuous BPR data, as
 580 they can be used to determine the long-term drift rate of the BPR and evaluated as a continuous
 581 record. Continuous pressure data also provide high-rate information useful for reducing aliasing
 582 and estimating long-period (daily to annual) oceanographic signals.

583 The disagreement between rates estimated using only individual surveys and rates from
 584 calibrated continuous data is attributed to aliased signals driven by physical oceanography. Most
 585 tidal analysis methods can typically remove up to 98% of the tidal signal, which still leaves several
 586 cm of uncertainty in each survey (Agnew, 2012; Pawlowicz et al., 2012). Additionally, any non-
 587 tidal effects from mesoscale eddies, currents, thermal fluctuations, or other causes are not
 588 addressed, which also contributes several cm of uncertainty in each survey. Advancements in
 589 satellite altimetry products, global and regional ocean models and hindcasts, CTD data, and nearby
 590 pressure sensor networks could improve our ability to characterize and account for oceanographic-

591 driven noise (Frederickson et al., 2019; Wilcock et al., 2021). Still, over shorter time periods (e.g.,
592 a few years) or when expected deformation rates are small (e.g., cm/year), the preferred method
593 includes the use of co-located BPRs. If significantly longer time periods (e.g., decades) are
594 expected or if expected deformation rates are large (e.g., tens of cm/year), then single point
595 absolute pressure surveys can suffice on their own. In both cases, the estimated rate uncertainties
596 will improve as the span of time between the first and last measurement increases.

597 These results demonstrate the capability of absolute seafloor pressure measurements for
598 seafloor geodesy. Establishing additional time series of absolute measurements would be valuable
599 for investigating other tectonic and oceanographic processes, such as the non-steric component of
600 global sea level rise. Our results do not yet allow us to clearly discern between different expected
601 vertical deformation rates associated with different models or studies that incorporate additional
602 geodetic data to produce stronger geophysical interpretations, but that is outside the scope of this
603 paper. However, the results do establish baseline vertical geodetic measurements in Cascadia and
604 that, when compared to similar absolute measurements spanning several decades in the future, will
605 be able to constrain secular vertical deformation rates.

606

607 **Acknowledgments**

608 This work was funded by NSF grants OCE 1558477 and OCE 1558468 and by a private donation
609 from Jerome Paros. We would like to thank, John Delaney, Deb Kelley, David Price, Joel White,
610 Heinz Wuhmann, and Michael Davis. We also thank the crews of the R/V Thomas G. Thompson,
611 R/V Roger Revelle, and R/V Sikuliaq, as well as the teams for ROV Jason II and ROV ROPOS.
612 The authors have no conflicts of interest for this publication.

613

614 **Open Research**

615 Data are available from the Marine Geoscience Data System (MGDS) at <https://www.marine-geo.org/index.php>
616 and from the UC San Diego Library Digital Collections at <http://library.ucsd.edu/dc/object/XXXXXXXXX>. The published data have been parsed from raw data
617 files and simply converted into physical units using manufacturer and lab calibrations. The raw
618 data and calibration data are not published because it would be impractical to parse through the
619 substantial amounts of ancillary data and formatting. However, the raw data, calibration data, and
620 other supporting data may still be requested from corresponding author, Matthew J. Cook, or from
621 author Glenn S. Sasagawa.

622

623

624

625 **References**

- 626 Agnew, D. C. (2012). SPOTL: Some Programs for Ocean-Tide Loading, *SIO Technical Report*.
627 UC San Diego: Scripps Institution of Oceanography.
628 <https://escholarship.org/uc/item/954322pg>
629
- 630 Atwater, B. F. (1987). Evidence for great Holocene earthquakes along the outer coast of
631 Washington State. *Nature*, 236(4804), 942–944, <https://doi.org/10.1126/science.236.4804.942>
632
- 633 Atwater, B. F., Musumi-Rokkaku, S., Satake, K., Tsuji, Y., Ueda, K., & Yamaguchi, D. K. (2005).
634 The orphan tsunami of 1700—Japanese clues to a parent earthquake in North America, *2nd*
635 *ed.: Seattle, University of Washington Press*, U.S. Geological Survey Professional Paper 1707,
636 135. <https://doi.org/10.3133/pp1707>
637
- 638 Bean, V. E. (1994). NIST pressure calibration service, *U. S. Department of Commerce, CODEN:*
639 *NSPUE2*, U. S. Government Printing Office, Washington, D. C., USA, Nat. Inst. Stand.
640 Technol. Spec. Publ., 250-39.
641
- 642 Chadwell, C. D. (2016). Initiation of GPS-Acoustics measurements on the continental slope of the
643 Cascadia Subduction Zone, Abstract T31C-2907 presented at the 2016 AGU Fall Meeting, San
644 Francisco, CA, 12-16 Dec.
645
- 646 Chadwick Jr, W. W., Nooner, S. L., Zumberge, M. A., Embley, R. W., & Fox, C. G. (2006).
647 Vertical deformation monitoring at Axial Seamount since its 1998 eruption using deep-sea
648 pressure sensors. *J. of Volc. and Geotherm. Res.*, 150(1-3), 313-327.
649 <https://doi.org/10.1016/j.jvolgeores.2005.07.006>
650
- 651 Fredrickson, E. K., Wilcock, W. S. D., Schmidt, D. A., MacCready, P., Roland, E., Kurapov, A.
652 L., Zumberge, M. A., & Sasagawa, G. S. (2019). Optimizing sensor configurations for the
653 detection of slow-slip earthquakes in seafloor pressure records, using the Cascadia Subduction
654 Zone as a case study. *J. of Geophys. Res.: Solid Earth*, 124(12), 13504-13531.
655 <https://doi.org/10.1029/2019JB018053>
656
- 657 Götze, H. J. (2011). International gravity formula. *Encyclopedia of Solid Earth Geophysics*, 611-
658 612. https://doi.org/10.1007/978-90-481-8702-7_102
659
- 660 Machida, Y., Nishida, S., Kimura, T., & Araki, E. (2020). Mobile pressure calibrator for the
661 development of submarine geodetic monitoring systems. *Journal of Geophysical*
662 *Research: Solid Earth*, 125, e2020JB020284. <https://doi.org/10.1029/2020JB020284>
663
- 664 Matsumoto, Y., Ishikawa, T., Fujita, M., Sato, M., Saito, H., Mochizuki, M., Yabuki, T., & Asada,
665 A. (2008). Weak interplate coupling beneath the subduction zone off Fukushima, NE Japan,
666 inferred from GPS/acoustic seafloor geodetic observation. *Earth, Planets and Space*, 60(6),
667 e9-e12. <https://doi.org/10.1186/BF03353114>
668

- 669 National Research Council (2012). Sea-Level Rise for the Coasts of California, Oregon, and
670 Washington: Past, Present, and Future. *Washington, DC: The National Academies Press.*
671 <https://doi.org/10.17226/13389>
672
- 673 Nooner, S. L., & Chadwick, W. W. (2009). Volcanic inflation measured in the caldera of Axial
674 Seamount: Implications for magma supply and future eruptions. *Geochem. Geophys.*
675 *Geosyst.*, 10(2), Q02002. <https://doi.org/10.1029/2008GC002315>
676
- 677 Nooner, S. L., & Chadwick, W. W. (2016). Inflation-predictable behavior and co-eruption
678 deformation at Axial Seamount. *Science*, 354(6318), 1399-1403.
679 <https://doi.org/10.1126/science.aah4666>
680
- 681 Paredes, X., Fandiño, O., Pensado, A. S., Comuñas, M. J. P., & Fernández, J. (2012). Experimental
682 density and viscosity measurements of di(2ethylhexyl) sebacate at high pressure. *The Journal*
683 *of Chemical Thermodynamics*, 44(1), 38-43. <https://doi.org/10.1016/j.jct.2011.07.005>
684
- 685 Paros, J. M., & Kobayashi, T. (2015a). Mathematical models of quartz sensor stability. Available
686 at: http://paroscientific.com/pdf/G8095_Mathematical_Models.pdf
687
- 688 Pawlowicz, R., Beardsley, B., & Lentz, S. (2002). Classical tidal harmonic analysis including error
689 estimates in MATLAB using T_TIDE. *Comp. & Geosci.*, 28(8), 929-937.
690 [https://doi.org/10.1016/S0098-3004\(02\)00013-4](https://doi.org/10.1016/S0098-3004(02)00013-4)
691
- 692 Polster, A., Fabian, M., & Villinger, H. (2009). Effective resolution and drift of Paroscientific
693 pressure sensors derived from long-term seafloor measurements. *Geochem. Geophys. Geosyst.*,
694 10(8). <https://doi.org/10.1029/2009GC002532>
695
- 696 Sasagawa, G. S., Cook, M. J., & Zumberge, M. A. (2016). Drift-corrected seafloor pressure
697 observations of vertical deformation at Axial Seamount 2013-2014. *Earth and Space Science*,
698 3(9), 381-385. <https://doi.org/10.1002/2016EA000190>
699
- 700 Sasagawa, G. S., & Zumberge, M. A. (2013). A self-calibrating pressure recorder for detecting
701 seafloor height change. *IEEE Journal of Oceanic Engineering*, 38(3), 447-454.
702 <https://doi.org/10.1109/JOE.2012.2233312>
703
- 704 Segawa, J., & Fujimoto, H. (1988). Observation of an ocean bottom station installed in the Sagami
705 Bay and replacement of the acoustic transponder attached to it, *JAMSTECTR Deep Sea*
706 *Research*, 256, 251-257.
707
- 708 Spiess, F. N., Chadwell, C. D., Hildebrand, J. A., Young, L. E., Purcell Jr, G. H., & Dragert, H.
709 (1998). Precise GPS/Acoustic positioning of seafloor reference points for tectonic studies.
710 *Physics of the Earth and Planetary Interiors*, 108(2), 101-112. [https://doi.org/10.1016/S0031-](https://doi.org/10.1016/S0031-9201(98)00089-2)
711 [9201\(98\)00089-2](https://doi.org/10.1016/S0031-9201(98)00089-2)
712

- 713 Stenvold, T., Eiken, O., Zumberge, M. A., Sasagawa, G. S., & Nooner, S. L. (2006). High-
714 precision relative depth and subsidence mapping from seafloor water pressure measurements.
715 *SPE Journal*, 11, 380-381. <https://doi.org/10.2118/97752-PA>
716
- 717 Walton, M. A. L., Staisch, L. M., Dura, T., Pearl, J. K., Sherrod, B., Gomberg, J., Engelhart, S.,
718 Trehu, A., Watt, J., Perkins, J., Witter, R. C., Bartlow, N., Goldfinger, C., Kelsey, H., Morey,
719 A. E., Sahakian, V. J., Tobin, H., Wang, K., Wells, R., & Wirth, E. (2021). Toward an
720 integrative geological and geophysical view of Cascadia Subduction Zone earthquakes. *Ann.*
721 *Rev. of Earth and Plan. Sci.*, 49(1), 367-398. [https://doi.org/10.1146/annurev-earth-071620-](https://doi.org/10.1146/annurev-earth-071620-065605)
722 [065605](https://doi.org/10.1146/annurev-earth-071620-065605)
723
- 724 Wang, K., & Trehu, A. M. (2016). Invited review paper: Some outstanding issues in the study of
725 great megathrust earthquakes—The Cascadia example. *J. of Geodynamics*, 98, 1-18.
726 <https://doi.org/10.1016/j.jog.2016.03.010>
727
- 728 Watts, D. R., & Kontoyiannis, H. (1990). Deep-ocean bottom pressure measurement: Drift
729 removal and performance. *J. Atmos. Oceanic Technol.*, 7(2), 296-306.
730 [https://doi.org/10.1175/1520-0426\(1990\)007%3C0296:DOBPMD%3E2.0.CO:2](https://doi.org/10.1175/1520-0426(1990)007%3C0296:DOBPMD%3E2.0.CO:2)
731
- 732 Watts, D. R., Wei, M., Tracey, K. L., Donohue, K. A., & He, B. (2021). Seafloor geodetic pressure
733 measurements to detect shallow slow slip events: Methods to remove contributions from ocean
734 water. *J. of Geophys. Res.: Solid Earth*, 126, e2020JB020065.
735 <https://doi.org/10.1029/2020JB020065>
736
- 737 Wearn, R. B., & Larson, N. G. (1982). Measurements of the sensitivities and drift of Digiquartz
738 pressure sensors. *Deep Sea Res. Part A. Oceanographic Research Papers*, 29(1), 111-134.
739 [https://doi.org/10.1016/0198-0149\(82\)90064-4](https://doi.org/10.1016/0198-0149(82)90064-4)
740
- 741
- 742 Wilcock W. S. D., Manalang, D. A., Fredrickson, E. K., Harrington, M. J., Cram, G., Tilley, J.,
743 Burnett, J., Martin, D., Kobayashi, T., & Paros, J. M. (2021). A thirty-month seafloor test of
744 the A-0-A method for calibrating pressure gauges. *Front. Earth Sci.*, 8, 600671.
745 <https://doi.org/10.3389/feart.2020.600671>
746